

# Imaging Spectroscopy in the Tokamak à Configuration Variable.

Martijn Fleuren

February 9 – June 5

2015

This report is written for obtaining the Bachelor of Engineering degree in applied physics, commissioned by The Hague University of applied sciences (HHS) in Delft, The Netherlands and carried out at the Dutch Institute For Fundamental Energy Research (DIFFER) in Eindhoven, The Netherlands.

My gratitude to Prof. Dr. M.R. De Baar and Dr. W. Vijvers for their guidance and feedback.

Supervision by Prof. Dr. M.R. De Baar (DIFFER) and Dr. R. Buning (HHS).

**THE HAGUE**  
UNIVERSITY OF  
APPLIED SCIENCES



# Summary

The purpose of this report is to assess the relevance of the measurement of the spectrally resolved distribution of radiation in tokamak boundary plasmas. This assessment is important and urgent in view of the recent ambition to design and construct a multi-camera configuration for hyper imaging spectroscopy<sup>1</sup> in the TCV tokamak in Lausanne, Switzerland. A collection of videos recorded in the visible light range – sometimes with a C-III filter – from earlier research was used and compared to single line of sight spectroscopic data and measurements from Langmuir probes.

The videos have been recorded with a high frame rate camera that was applied for plasma boundary detection and for real time plasma position control. The first step in project was to index the videos in a database, which is driven by SQL – this provides superior flexibility and speed over a spreadsheet. Various phenomena were identified in which a clear variation in the distribution of the intensity over the plasma can be observed. Then, a list containing the IDs of the recordings was constructed from the database so that sufficient review material was available for each phenomenon. Four phenomena were identified as potential study cases. These are *a)* data from two cameras one of which is using a C-III filter while the other is observing visible light are used to identify a significant spatial displacement of the hydrogen and carbon lines. *b)* Emitting structures in the plasma boundary, reminiscent of *MARFEs* [1], have been observed. *c)* Quasi-toroidal variations in the intensity are observed, reminiscent of the effects of micro-turbulence. *d)* During some discharges, *plasma detachment* is thought to be observed by a variation in intensity that shifts over a leg towards the divertor.

Examples of these phenomena will be shown in the report. For further analysis – given the availability of the data at TCV – it was decided to proceed with the C-III data and the alleged detachment data for further analysis.

The temperature was estimated based on the assumption that the temperature of the plasma boundary is the same as the photon temperature of their main contributing emission component. With MATLAB image processing, the distance between the apparent boundaries of C-III and H- $\alpha$  radiation have been estimated. With those results, the spatial ( $\nabla T_x = 0.77 \text{ eV m}^{-1}$ ) gradient and the temporal evolution thereof has been estimated.

For the alleged detachment cases, a detailed comparison with measurements of additional diagnostics was carried out. Langmuir probe data shows sudden changes in the saturation current to the divertor and the perpendicular power load on the divertor surface. This coincides with a reduced heat- and particle

---

<sup>1</sup>HIS is explained in Appendix B.

load. It can be concluded that detachment is occurring and that the heat load is reduced. Spectrally resolved data shows that the instant that the plasma detaches from the divertor, the spectral intensities change as well. Spectral, spatial and temporal solutions can thus be found for this phenomenon.

The progress of this work was hampered due to a mismatch of ID numbers of the discharges or due to saturated signals from the Langmuir probes in some cases. This was solved by combining data from different yet similar discharges. With this caveat, it is demonstrated that temporal, spectral and spatial data is *crucial* to understand and – most likely – control the plasma boundary.

# Contents

|          |  |           |
|----------|--|-----------|
| <b>1</b> | <b>Introduction</b>                        | <b>6</b>  |
| 1.1      | Nuclear fusion . . . . .                   | 6         |
| 1.2      | Principle and plasma equilibrium . . . . . | 6         |
| 1.3      | The nuclear fusion reaction . . . . .      | 7         |
| 1.4      | Requirements . . . . .                     | 7         |
| 1.5      | Tokamak . . . . .                          | 8         |
| 1.6      | Modes of operation . . . . .               | 10        |
| 1.7      | Problem Statement . . . . .                | 11        |
| <b>2</b> | <b>Imaging an emitting surface</b>         | <b>14</b> |
| 2.1      | Phenomena identification . . . . .         | 14        |
| <b>3</b> | <b>Diagnostics</b>                         | <b>16</b> |
| 3.1      | Langmuir probe . . . . .                   | 16        |
| 3.2      | Ocean optics spectroscope . . . . .        | 16        |
| <b>4</b> | <b>Theory</b>                              | <b>18</b> |
| 4.1      | Detachment . . . . .                       | 18        |
| 4.2      | Temperature Gradient . . . . .             | 18        |
| <b>5</b> | <b>Results</b>                             | <b>20</b> |
| 5.1      | Detachment . . . . .                       | 20        |
| 5.2      | Temperature gradient . . . . .             | 22        |
| <b>6</b> | <b>Summary and conclusion</b>              | <b>25</b> |
| 6.1      | Discussion . . . . .                       | 25        |
| <b>A</b> | <b>Database structure</b>                  | <b>27</b> |
| A.1      | SQL and databases . . . . .                | 27        |
| A.2      | Events . . . . .                           | 28        |
| A.3      | Metadata . . . . .                         | 29        |
| A.4      | Raw . . . . .                              | 30        |
| <b>B</b> | <b>Camera system</b>                       | <b>31</b> |

# Chapter 1

## Introduction

Nuclear fusion and the plasma equilibrium are described in this chapter as well as the problem statement at the end. The imaging of the plasma boundary using tangential cameras is explained in Chapter 2, regions of low sensitivity and limitations of the imaging are emphasised. The observed phenomena are introduced in Chapter 4 and their physical analysis is carried out in Chapter 5. Conclusions, recommendations and the discussion follow in Chapter 6. In the appendix the database and its structure will be explained, and a brief description will be given about the camera system.

### 1.1 Nuclear fusion

Global energy demands are rising in both quantity and quality. Current production relies on burning fossil fuels for heat. This form of energy comes easily because no extensive processing is required, and the plants are already established. The supply of these resources is finite which makes production unsustainable, in addition to being hazardous for the environment [2].

*Nuclear fusion* is a candidate to solve the demand for a sustainable and clean source of energy. It is a promising source because the power output per unit area is high and only little fuel is required. It distinguishes itself from other solutions by being clean, and having a good yield. In Cadarache – a French research centre – the preparations are taking place for an international experimental reactor: ITER. It will roughly yield  $1.2 \text{ kW m}^{-2}$  [3].

The development for commercial fusion reactors is ongoing, reactors are experimental and do not yet meet efficiency requirements which makes them expensive and thus economically non-viable.

### 1.2 Principle and plasma equilibrium

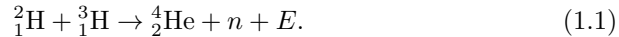
In thermonuclear fusion reactors, a hot hydrogen fuel is confined with magnetic fields. This fuel has a temperature of several tens of millions degrees, and is fully ionised. The fuel is said to be in the plasma state.

The magnetic field in which the plasma is confined is organised in flux surfaces that are toroidally symmetric and have a constant magnetic flux. The plasma is confined inside the last closed flux surface (LCFS) and in most cases

this region does not emit light. Outside the LCFS, field lines are *not* closed but are connected to the vessel wall. This layout is also referred to as the plasma equilibrium [4]. A parallel gradient in temperature, density and emission is set-up along the field lines from the solid wall to the LCFS. This is the region in which light is emitted.

### 1.3 The nuclear fusion reaction

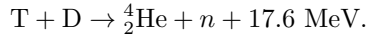
The reaction to produce energy from fusing hydrogen is



From this point,  ${}^3_1\text{H}$  is referred to as T for *Tritium* and  ${}^2_1\text{H}$  as D for *Deuterium*. Deuterium occurs at a rate of  $\sim 155$  ppm in seawater which is a virtually unlimited supply, but tritium does not occur in nature because it decays ( $\lambda = 1.83 \cdot 10^{-9} \text{ s}^{-1}$ ,  $t_{1/2} = 12.32$  years).



Producing sufficient amounts of tritium has become one of the challenges to overcome on the road to commercial fusion reactors. A neutron from Reaction (1.1) can be used to produce the tritium from Lithium-6, a part of the reaction will thus be cyclic.



Note that the neutron in the first part originates from the third part of the same reaction and that deuterium is *externally* added in the second part.

To avoid radioactive contamination of the reactor vessel, the TCV runs experiments with deuterium-deuterium fusion (DD-mode) only and does *not* produce energy. All the power that is deposited in the reactor is exclusively from external systems.

### 1.4 Requirements

In order for Reaction 1.3 to occur, the nuclei have to get so close to each other that they fall into a potential well caused by the strong force (Figure 1.1). Before this can occur, nuclei face the Coulomb barrier because they are like-charged. This barrier is overcome by doing work which is yielded through kinetic energy  $E = k_B T = \int_{\infty}^{\rho} F dr = 100 \text{ keV}$  or  $1.16 \text{ GK}$ , where  $\rho$  is the critical distance of around  $14 \text{ fm}$ . The desired temperature is much lower ( $10 \text{ keV}$ ) than the temperature that guarantees fusion for every nucleus, therefore the reaction has to rely on more than just temperature.

There is a chance for the nuclei to tunnel through the Coulomb barrier, the probability of which is proportional to the density  $n$ , and decreases with the width of the barrier. By increasing the particle density and raising them high enough on the barrier, sufficient amounts of nuclei will be able to tunnel and fuse to yield energy which sustains the reaction.

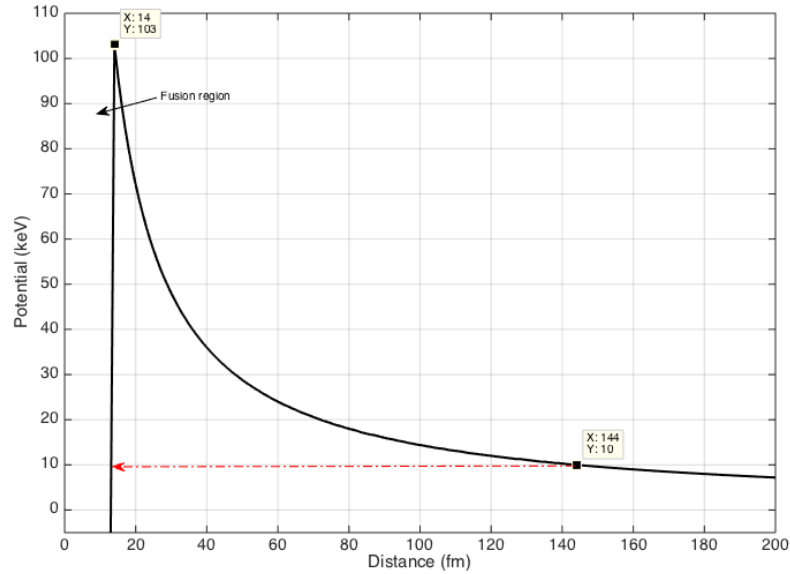


Figure 1.1: The nuclear potential of two Hydrogen nuclei. The red arrow depicts quantum tunneling which allows for fusion at lower potentials.

The reactor yields energy if the temperature  $T$  and density  $n$  are high enough. In addition, the energy confinement time should be as high as possible. The confinement time  $\tau$  is a measure of this principle and can be calculated with power in- and output. In steady state, the power in- and output are equal  $P_{\text{in}} = P_{\text{out}}$ , and there is an amount of energy  $E$  stored inside the plasma. The time constant  $\tau$  can then be calculated with  $\tau = E/P$ .

The product of these three values is known as the Lawson-criterion and is a figure of merit for the performance of the reactor.

## 1.5 Tokamak

A successful magnetic confinement device is the tokamak. It was first developed as ‘toroidal chamber with magnetic coils’ during the 1950’s in Russia. It uses magnetic coils to confine and control the plasma inside a torus shaped vessel (Figure 1.2).

In this section, components that are relevant for this report will be briefly described.

### Limiter

In early tokamaks, the plasma has physical contact with the wall of the vessel. The heat of the plasma releases atoms from the wall, which then blend with the fuel and degrade its purity. These impurities will absorb energy from the plasma and radiate it away, having a cooling effect. Damage to the wall and reduced plasma performance have led to the design of a device that minimises

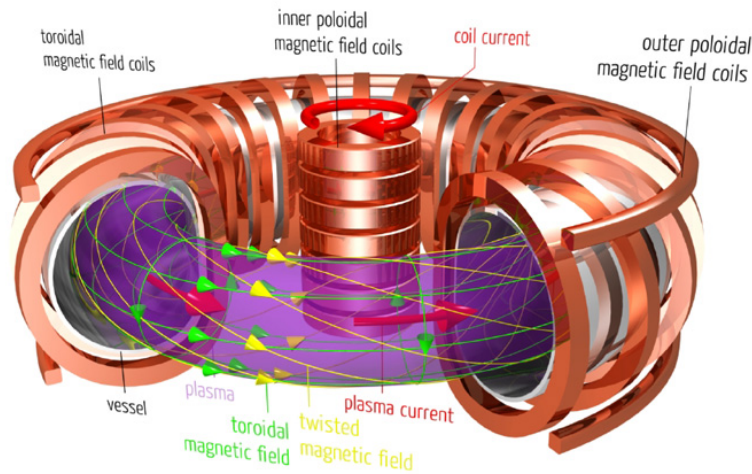


Figure 1.2: A schematic of a tokamak. Courtesy of Max-Planck institut für Plasma-physik

plasma surface interactions by limiting the plasma radius to a smaller radius than the containing vessel. Such a device is called a *limiter*.

Due to a concentration gradient in the plasma, particles will diffuse outward and eventually cross the LCFS to a region with open field lines. This forms a thin layer, called the scrape-off layer (SOL), which lays outside the radius set by the limiter. All the particles and heat in the SOL will eventually be deposited on the limiter surface and due to a small width ( $\sim 2$  cm), the particle and heat fluxes will be large.

The main advantage of a limiter is its simplicity. The disadvantages are, that even components that are designed to contact the plasma and receive high particle and heat fluxes will release impurities, break down and cause sputtering.

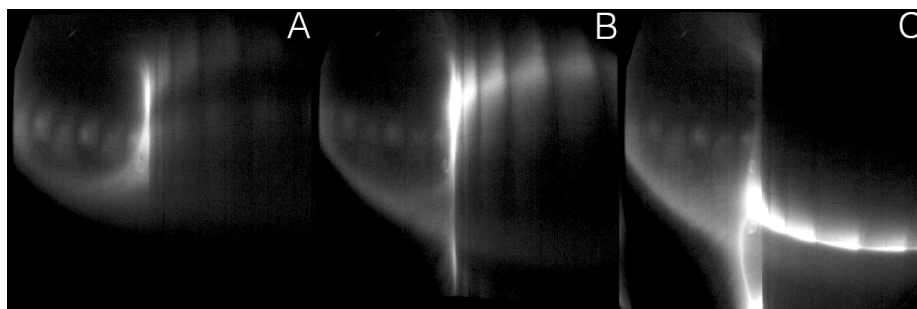
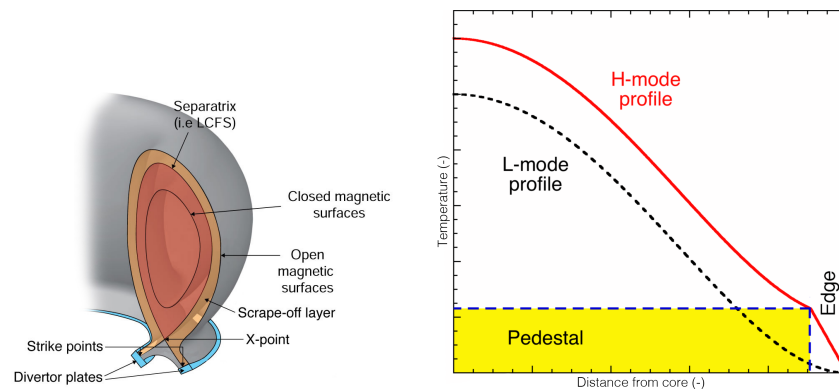


Figure 1.3: a) Limited plasma, pseudo-circular in the poloidal plane. b) Limited, shape is altered by magnetic pressure. c) Diverted plasma, the x- and strike-points are clearly visible.

## Divertor

The divertor can be thought of as the exhaust of the reactor. It allows for fuel composition control while the reactor is running, and access to H-mode. A diverted plasma has a different shape than a limited plasma, this shape is forced on the plasma to create a ‘null’ or ‘x-point’ (Figure 1.4a). Legs of the plasma reach from the x-point towards the divertor plates, and connect on the strike points. These points on the plate endure extreme heat and particle fluxes ( $\sim 200 \text{ MW m}^{-2}$ ), unmanageable even with the best cooling technology.



(a) Simplified model of a diverted plasma with a single null (SN) or x-point.

(b) Modes of the plasma. If the edge becomes too steep, the boundary will collapse and release energy from the pedestal. Courtesy of FusionWiki.

Figure 1.4

## 1.6 Modes of operation

Plasma can operate in two modes of confinement: L- and H-mode for ‘low-’ and ‘high energy confinement’ respectively. The name cognitively dictates how much energy is stored in the plasma at a given moment. Due to the Lawson-criterion explained in Section 1.4, it is desired to store as much energy as possible in the plasma, so that the confinement time can be increased. A significant increase – typically a factor of 2 – will result from plasma in H-mode [5].

The temperature profile of H-mode is roughly equivalent to L-mode from the core to the boundary (Figure 1.4b), but is very steep at the boundary. Because the profiles are roughly equivalent, the extra energy stored can be approximated by a rectangle known as the ‘pedestal’.

The temperature gradient at the boundary of a H-mode plasma may become so steep that the plasma collapses and releases energy from the pedestal. This event, which seems to result in a violent flash, is known as an edge-localised mode (ELM) and can be seen in Figure 1.5.

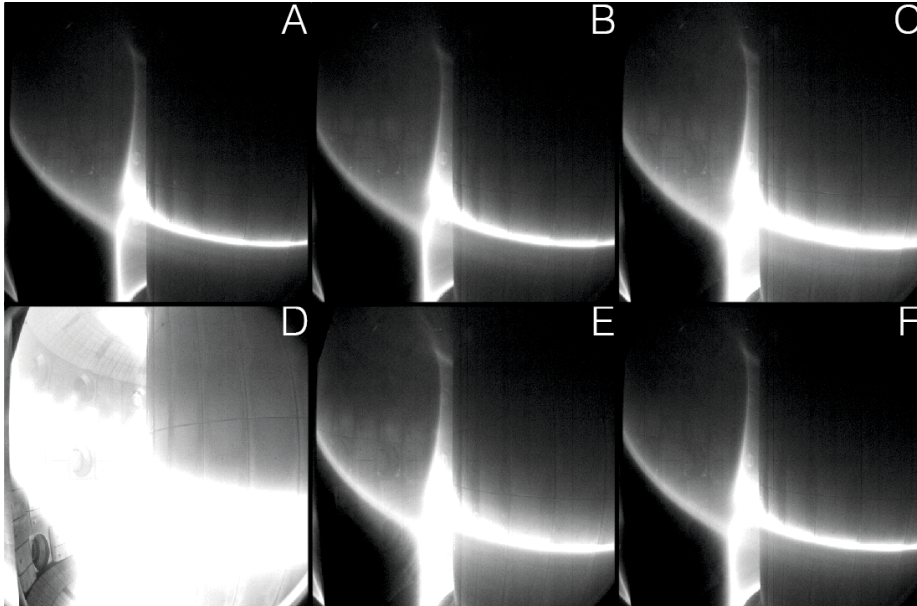


Figure 1.5: An example of an ELM in shot 48825 between frames 378 and 383. The frame rate of this shot is unknown but should be around 200, implying that the time scales are around the order of  $5 \text{ ms frame}^{-1}$

## 1.7 Problem Statement

Intensity imaging displayed high sensitivity to tangency of sight lines to the LCFS. An inversion method – dubbed ‘OFIT’ – was derived based on the assumption that light originates from where the sight line of a pin-hole is tangent to the plasma surface [6] and showed excellent and fast inversion from image to plasma boundary coordinates. It was also shown that using this boundary as a constraint, a fast and non-iterative method for equilibrium-estimation could be set-up [7]. The OFIT procedure was also used to determine parts of the plasma boundary in real-time for position control [8].

During the development of this method, nearly a thousand videos of full discharges were recorded. A lot of additional information seems to be present in these videos, notably associated with the distribution of radiation (DR) and its temporal evolution. Assuming that the sensitivity to tangency holds, the main question will be *‘Is it possible to interpret the distribution of radiation physically?’*.

The phenomena that have been identified in the experimental data are: *a)* In discharges that were recorded with two cameras using H- $\alpha$  and C-III filters, a misalignment of the hydrogen and carbon line intensity have been identified. This can be exploited to estimate the *local temperature gradient* inside the plasma boundary per image. By applying the estimation to a video, a temporal estimation can be made. This is an extension to the OFIT code for extracting the boundary position. *b)* Emitting structures in the plasma boundary that seem to rotate poloidally are observed. These observations are the reminiscent of *MARFEs* [1] and it will be attempted to identify the conditions under which this phenomenon is observed. The results will be compared to conditions under

which MARFEs would theoretically be expected (Figure 1.6). *c*) Sometimes, seemingly quasi-toroidal variations in the intensity are observed. These are reminiscent of the effects of micro-turbulence, Using three-dimensional modelling it will be attempted to synthetically image micro-turbulent structures in the plasma boundary (Figure 1.7). *d*) During some discharges, *detachment* is thought to be observed by a variation in intensity that shifts over a leg towards the divertor (Figure 1.8).

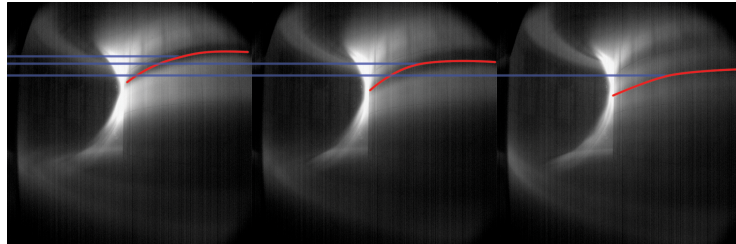


Figure 1.6: Depiction of what an alleged MARFE in shot #49216, the structure that is visible rotates helically along the torus. The structures position is depicted by the red line and its vertical position by the blue lines.

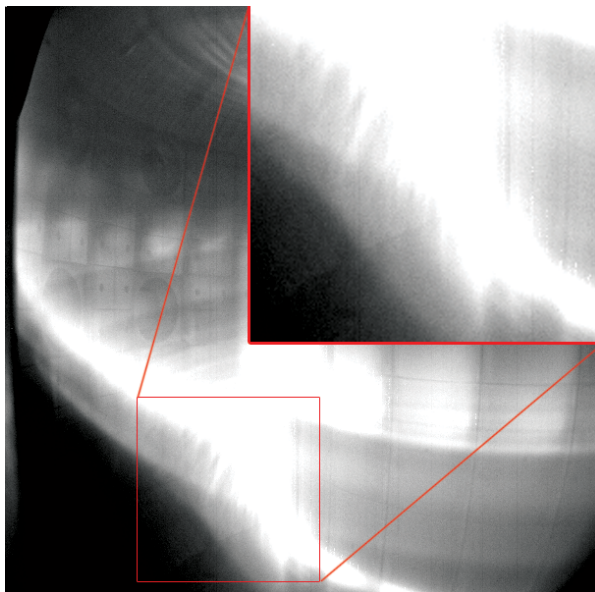


Figure 1.7: Alleged microturbulence in shot #48966 frame 375, the filaments that are observed on the outer mantle are the points of interest

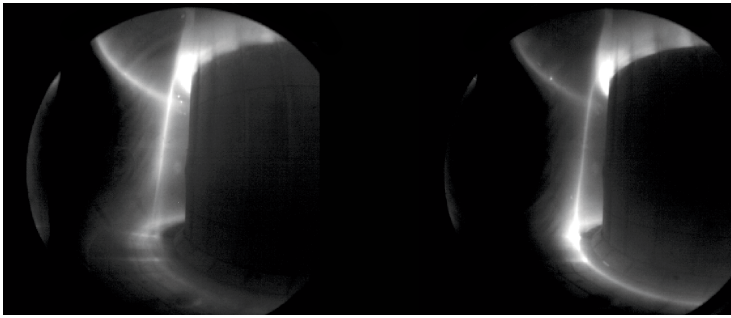


Figure 1.8: Detached plasma in shot #46111, times are 1.52s and 1.57s ( $\Delta t = 0.05$ s).  
Left: Plasma is detached. Right: Plasma is re-attached.

## Chapter 2

# Imaging an emitting surface

An image is a two dimensional projection. The projection is set-up from a rectangular grid of pixels (CMOS sensor LUPA-1300-2) which accumulate a voltage proportional to the amount of photons that hit its surface during the exposure time. The camera that is observing the plasma, collects the most light from the plasma boundary. This is because it is highly sensitive to its sight lines being tangent to the plasma surface (Figure 2.1). This feature has been used to detect the plasma boundary[6], and to reconstruct a 3D object based on the assumption of toroidal symmetry. The boundary detection has been applied to control the plasma position in real time in the TCV[8].

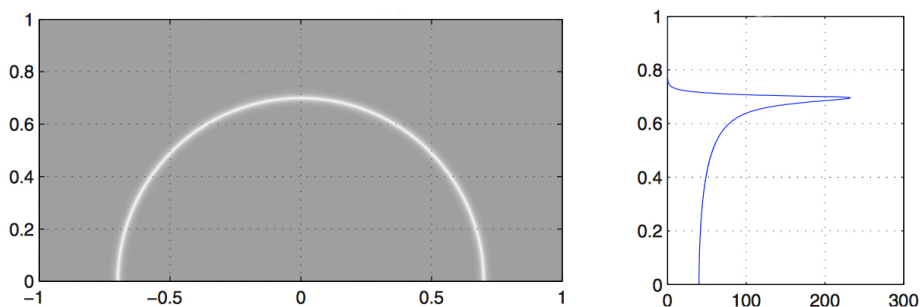


Figure 2.1: Left: Plasma emission in the equatorial plane. Right: Corresponding intensity. Courtesy of G. Hommen [6]

### 2.1 Phenomena identification

Work that was carried out previously did not focus on the distribution of radiation (DR). Phenomena that are related to the DR are however visible in the recordings, and remain to be interpreted manually. The question becomes if these recordings are indeed eligible to be interpreted with respect to the DR: ‘Can images of the poloidal plane be used to interpret the static and temporal distribution of radiation over the entire surface, and can distinctions be made in wavelength?’

Examples of clearly visible phenomena are: a) The transition from L- to

H-mode seems to occur when the boundary suddenly gets more sharply defined. In L-mode, the primary contribution to the radiation comes from H- $\alpha$ , whereas in H-mode the primary contribution is C-III. The mean position of the boundary also shifts inward when the latter is radiating. This could be used to crudely estimate the temperature gradient of the boundary to within an order of magnitude. *b)* Intensity shift along the divertor leg towards the divertor. This may indicate plasma detachment. Additional data from the TCV team and comparison to similar shots will reveal if this is indeed the case and if the heat flux on the divertor is significantly reduced.

# Chapter 3

## Diagnostics

In this chapter, an overview and description will be given of the instruments that were used to obtain the measurements. One diagnostic source are the video recordings which have been described in Chapter 2. The camera system will be briefly described in Appendix B.

### 3.1 Langmuir probe

A Langmuir probe is a device that is used to determine the density, temperature and potential of a low temperature plasma (up to a few eV). It was initially designed in an attempt to measure the voltage distribution of a gas discharge.

A probe consists of a bare metal wire that is inserted into the plasma, where there are currents of electrons and ions. Because of the difference in mass, electrons are much faster than ions at the same temperature. Due to this difference in velocity, the electron current to the probe is higher than the ion current. The net current must be zero, therefore the probe drifts to a negative potential so that it repels electrons and attracts ions. The potential of the probe is thus lower than the potential of the plasma.

The voltage of the probe is swept from a negative to a positive voltage, during which the I-V characteristic of the probe is obtained. From the shape of the I-V characteristic, the particle density and plasma temperature can then be deduced

### 3.2 Ocean optics spectroscope

A spectroscope composed of five different spectrometers is placed in the TCV for measuring different parts of the atomic spectrum emitted by particles in the plasma within one line of sight. The configuration of this system can be seen in Figure 3.1 and the wavelength specifications in Table 3.1. The acquisition frequency is 100 Hz.

The general remarks of the system that have been provided are *a)* The system has not been maintained since mid 2011. *b)* There is an uncertainty on the wavelength calibration of up to 5 nm. *c)* At some view lines, filters have been installed in front of the collection optics which may alter the efficiency of the spectrometer. The characteristics of the filter is currently unknown. *d)* The

Table 3.1: Specifications of the Ocean Optics system. Positions correspond with the positions in Figure 3.1

| Position | Wavelength Range (nm) | Resolution  |
|----------|-----------------------|-------------|
| 1        | 200 – 500             | –           |
| 2        | 600 – 735             | –           |
| 3        | 200 – 800             | –           |
| 4        | 200 – 800             | $\geq 3$ nm |
| 5        | 350 – 1000            | $\geq 3$ nm |

integrating cone for each view line has not been measured, this can change between view lines because the lenses and apertures are different between view lines.

The different positions of the spectrometers can be utilised when analysing detachment. If detachment is taking place, the spectrometers at different positions should measure a peak intensity that was previously located elsewhere in the spectrum.

With this instrument, a temporal analysis of the spectrum was realised. The results of which can be found in 5.1.

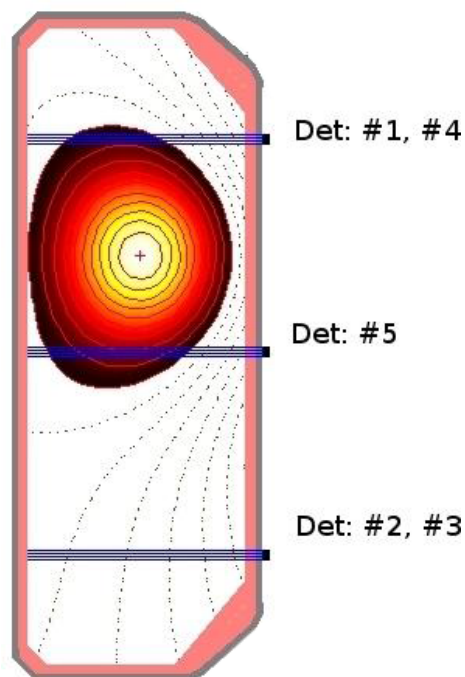


Figure 3.1: Ocean Spectrometry system setup in the poloidal plane. The position numbers correspond to the numbers in Table 3.1

# Chapter 4

## Theory

In this chapter the theory behind the phenomena will be explained, formulas for quantitative and / or qualitative analysis will also be derived..

### 4.1 Detachment

When a diverted plasma enters a detached state, it is no longer physically connected to the divertor. Being able to control this state, enables controlling of the heat flux on the divertor surface. This surface may receive a heat and particle flux of  $\sim 200 \text{ MW m}^{-2}$ , which cannot be cooled even with the best cooling equipment available ( $\sim 10 \text{ MW m}^{-2}$ ). It is desired to reduce the flux on the divertor, but without reducing the performance of the reactor.

A proposed solution is reduction of the heat flux with radiation: Injecting a gas in the reactor causes the plasma – ions and electrons – to excite the gas by colliding with its atoms. When these atoms return to a lower energy state they emit a photon. Energy is thus radiated away and the heat flux on the divertor is reduced. The placement of this gas is important. Gas placed inside the hot plasma core reduces the heat flux on the divertor but also reduces the overall performance – Due to the Lawson criterion from Section 1.4. The gas will in practice be placed between the divertor leg and the divertor plate, where it will act as a cool buffer layer. The radiation will be isotropic and roughly homogeneous, so the energy that is removed from the heat flux is spread out evenly over the entire vessel wall to levels that are manageable by the heat extraction systems.

If the videos indeed show detachment, it becomes possible to detect the state optically and carry out in depth analyses to further explore the possibilities of radiative cooling. This may solve the heat flux problem on the divertor. A qualitative analysis will be carried out by comparing the saturation current density on the Langmuir probes that are close to the strike point, and the perpendicular power on the divertor plate.

### 4.2 Temperature Gradient

The heat flux through the boundary of the plasma dictates the quality and the stability of the confinement regime. With an estimate of the temperature

gradient, the perpendicular heat flux through the LCFS can be estimated and with that the position on the confinement stability curve. If the temperature gradient can be estimated in real time, it will be known at any time if the plasam is in H- or L-mode.

According to kinetic theory  $E = \frac{1}{2}kT$  per degree of freedom, of which there is only one in a tokamak, this relation can be used to get a figure in kelvin, but plasma- and electron temperature are often expressed in eV. The temperature of the particle that emits the photon can be estimated by assuming that particles are excited by collisions only and that their energy is converted to a photon according to  $E = h\nu = \frac{hc}{\lambda}$ .

Expressing a temperature in eV is done by simply dividing an energy – in this case the photon energy – by  $e$

$$T_{\text{eV}} = \frac{hc}{\lambda e}. \quad (4.1)$$

The temperature of the boundary when the primary contribution comes from H- $\alpha$  ( $\lambda = 656$  nm) is 1.89 eV and when it comes from C-III ( $\lambda = 466$  nm), the temperature is 2.66 eV. The spatial gradient  $\nabla T_x$  can be estimated when the apparent distance between these two boundaries is known. A temporal gradient  $\nabla T_{x,t}$  estimation can be made by expressing the spatial temperature gradient as a function of time.

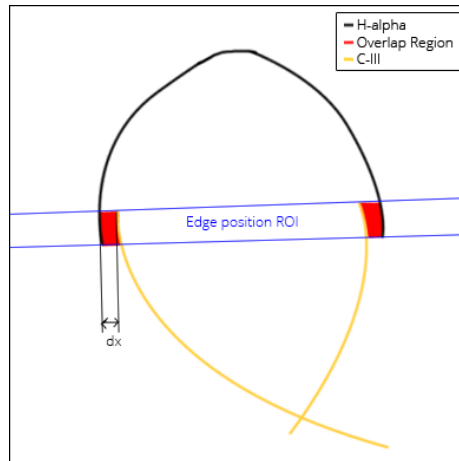


Figure 4.1: The principle of determining the plasma boundary temperature gradient. Within the region of interest (ROI), the position of the plasma is determined to extract  $\Delta x$  (red region)

## Chapter 5

# Results

The results and elaborations will be presented in this chapter. One of the results is the database, it cannot be printed but details can be read in Appendix A. The other results are the alleged detachment and the temperature gradient. The timespan of the project was too narrow to answer the remaining questions about microturbulence and MARFEs.

### 5.1 Detachment

The IDs of the recordings that show a shift in intensity have been sent to the TCV team in request of additional data for those shots. However, none of them had eligible measurements due to saturated signals. Instead, a sufficient amount of data from similar recordings (the plasma was in the same state) has been provided. In Figure 5.1, a plasma can be seen in both detached and reattached states.



Figure 5.1: Detached plasma in shot #46111, times are 1.52s and 1.57s ( $\Delta t = 0.05s$ ). Left: Plasma is detached. Right: Plasma is re-attached.

## Time analysis

Re-attachment seems to occur when the gas flux is reduced by closing a valve – This can be seen in Figure 5.2 in the first graph. The other parameters that are plotted in the same figure – From top to bottom – are: The density (green line in the same graph as the gas flux), ion saturation  $J_{\text{sat}}$  as measured by a Langmuir probe, perpendicular heat flux through the LCFS  $q_{\perp}$ , the electron temperature  $T_e$  and the plasma pressure  $p_e$ . The red line is drawn on the instant that the gas valve closes which leads to a reduced density. The ion saturation current, perpendicular heat flux toward the tiles and plasma pressure increase with a factor  $\sim 2$ . This supports the statement that the plasma is in a detached state and is re-attaching. It also strongly motivates that this phenomenon can be observed with a tangential camera configuration.

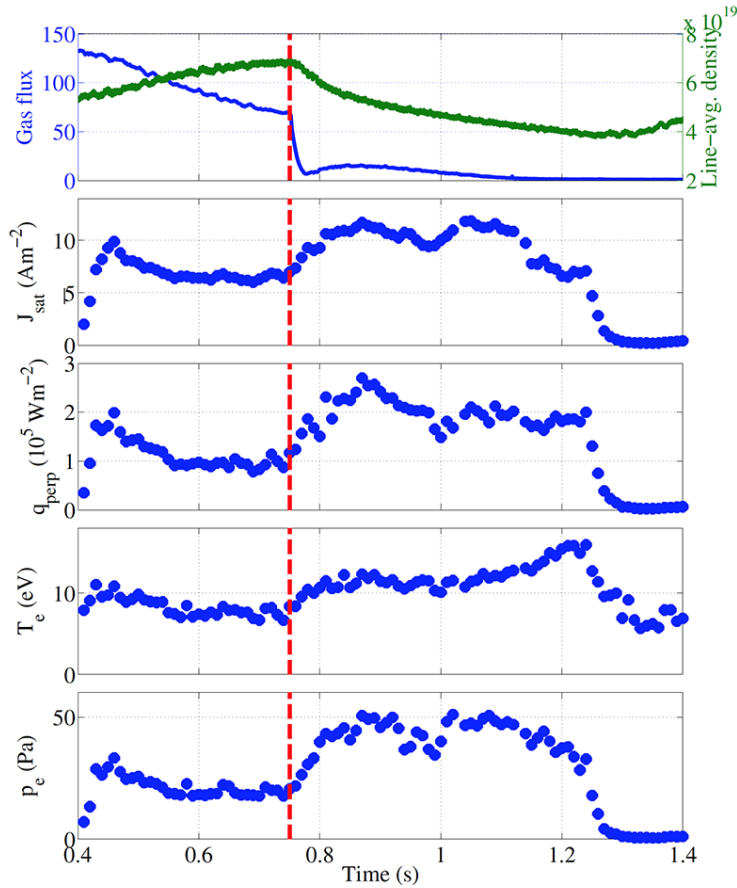


Figure 5.2: Plasma parameters during shot #44819. The gas flux is visible in the first graph. The time that the gas valve closes is indicated by the red line. It is clear that the gas flux influences the other parameters.

## Spectral analysis

A spectral analysis of the same discharge (#44819) with the Ocean Optics Spectrometer (Figure 3.1) displays shifts in relative intensity right around the time that the gas valve closes (Figure 5.3). Intensities on  $\lambda \approx 385$  nm and  $\lambda \approx 390$  nm reach approximately the same value, the latter after the valve closes. More of these pairs can be seen in the same figure around  $\lambda \approx 410$  nm and  $\lambda \approx 430$  nm. The latter switches in the opposite direction.

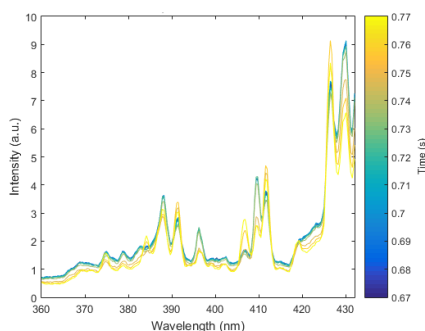


Figure 5.3: The spectrum of the plasma at position 3 (Figure 3.1) in an arbitrary unit, color coded for time, around the time that the gas valve closes. It can be seen that specific lines show a reduced intensity, while others show an increase in intensity.

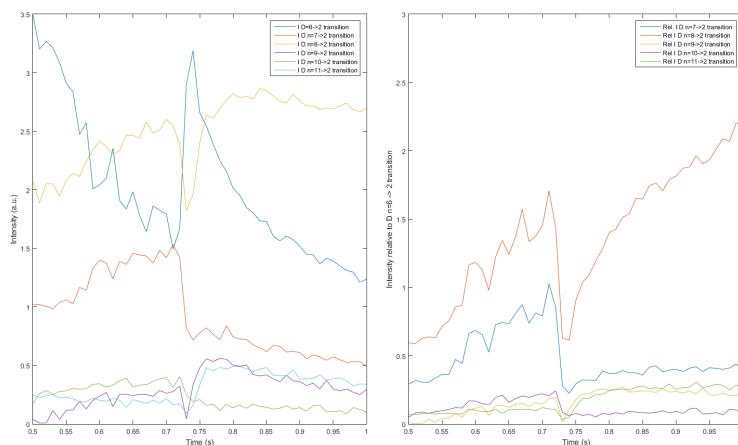


Figure 5.4: Intensities of high- $n$  Balmer lines. Left: Intensity of Balmer lines and their temporal evolution expressed in an arbitrary unit. Right: Intensities relative to the  $n_{6 \rightarrow 2}$  transition. Remarkably, the changes in intensities are sudden transitions. This is consistent with the sudden movement of the radiating front in the divertor.

## 5.2 Temperature gradient

The position of the plasma boundary is tracked with the OFIT Z-observer, which calculates the boundary position from the video at regular time-intervals and

returns a single precision float array in meters. This data is used for further analysis (after filtering), a plot of the filtered position data can be seen in Figure 5.5.

Before the analysis can be done, the data has to be filtered. *a)* The time resolution of the C-III data was twice as high as that from the H- $\alpha$  data resulting in arrays that were different in size. These were matched up using corresponding values for the time and the intermediate points from the C-III data were discarded. *b)* The time on both arrays was offset by  $-0.018$  s which was corrected by offsetting every point by  $0.018$  s *c)* At the start and the end of a discharge, the plasma is unstable and the position cannot be determined with accuracy. The time interval was selected to be  $0.40 \text{ s} \leq t \leq 1.40 \text{ s}$ . This has been done manually and somewhat arbitrarily so that plasma within the interval is guaranteed to be pseudo-stable. *d)* There are very large spikes that deviate from the data by a factor 200, these skew the results of the mean. To achieve a ‘low-pass filter effect’, the matlab function `medfilt1()` was applied to rid the data of spikes.

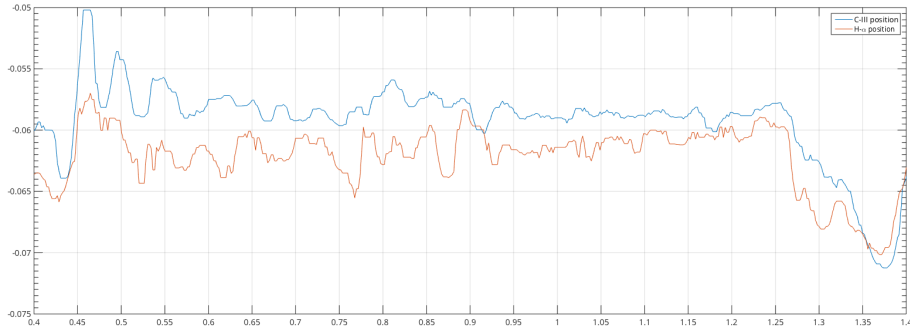


Figure 5.5: A plot of the filtered data from the Z-observer. A clear difference in apparent boundary position is visible.

The mean and standard deviations for this observation are  $\bar{x} = -59.4$  mm,  $\sigma = 3.5$  mm and  $\bar{x} = -62.3$  mm,  $\sigma = 3.0$  mm for H- $\alpha$  and C-III respectively, with a mean difference of 2.8 mm. These values have been calculated over the filtered data with the built in matlab functions `nanmean()` and `nanstd()` to compensate for undefined results in the array without having them impact the outcome. The difference in photon temperature calculated with (4.1) is 0.77 eV. With the mean difference between the apparent boundaries known, the mean spatial temperature gradient can be calculated  $\nabla T = 0.77/0.0029 = 276 \text{ eV m}^{-1}$ .

A plot that displays the temporal evolution of the gradient can be made by calculating the difference between the boundary for every point in time and evaluating what the temperature gradient is at that point. The results of which can be seen in Figure 5.6

Taking the mean over all these points, yields the correct average spatial gradient of  $188 \text{ eV m}^{-1}$

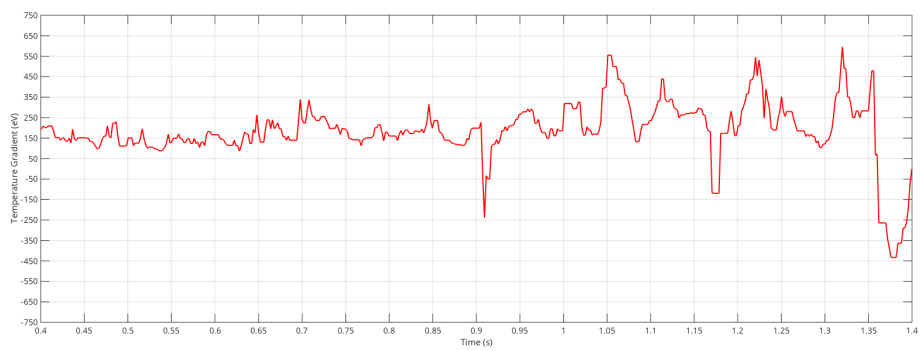


Figure 5.6: Temporal evolution of the temperature gradient. Note that the fluctuations in the signal increase after 0.9 s. This is associated with a steady reduction of the line-separation (Figure 5.5), which leads to instability of the calculated derivative.

# Chapter 6

## Summary and conclusion

Starting with a set of videos, the question stated was if it would be possible to interpret their distribution of radiation (DR) from these videos and if the DR could be resolved spectrally. With additional data obtained from the team at TCV, a time- and spectral analysis were made. From the time analysis it can be concluded that detachment is indeed occurring and that detachment can be sensed with a tangential camera configuration. The spectral analysis showed that the data can be spectrally resolved which motivates a multi-camera configuration for hyper imaging spectroscopy. The second question was if it was possible to calculate the temperature gradient from the videos. With a static photon temperature approach and OFIT, the spatial temperature gradient and the temporal evolution thereof has been estimated.

### 6.1 Discussion

Not all the proposed questions could be answered and the viability analysis about MARFEs and microturbulence remains. Some of the methods can be extended or more accurate measurement can be achieved by altering the processing technique. The goal of this chapter is to explore and discuss what can be done to improve and / or extend this research.

#### Temperature gradient

The temperature gradient was estimated in Section 4.2. A negative temperature gradient can be seen in the temporal evolution graph (Figure 5.6), which is physically not possible because the temperature on the outside of the plasma would then be higher than on the inside.

An extension to the estimation technique can be made when the pixel value is used to retrace the spectral emission of the plasma.

To achieve this, the amount of photons on each pixel is calculated from its digital value  $Q_{i,j}$ , which is a measure of the time integral of the illuminance over its surface. The value of each pixel has been quantised by an analogue to digital converter (ADC), which linearly distributes a voltage between 0 volts and a reference voltage. The pixel voltage can be calculated with

$$V_{\text{px}} = V_{\text{ref}} \frac{Q_{i,j}}{2^b - 1}, \quad (6.1)$$

where  $b$  is the amount of bits, and  $V_{\text{ref}}$  is the internal voltage reference of the ADC of 2.5 volts. The reference voltage is quantised in steps of  $2.44 \text{ mV bit}^{-1}$ , because of this the measurement can be no better than  $\pm 1.22 \text{ mV}$ , which is half of the least significant bit (LSB). Quantisation also introduces a noise spectrum with a signal to noise ratio (SNR) of  $6.02 \cdot b \text{ dB}$ .

The data sheet of the image sensor provides insight on the linear pixel sensitivity ( $S = 25 \text{ V lux}^{-1} \text{ s}^{-1}$ ). The exposure time  $t_e$  is assumed to be without jitter. A relation that relates the illuminant spectrum  $E_\nu$  to the voltage can now be set-up and is equal to

$$V_{\text{px}} = St_e E_\nu = V_{\text{ref}} \frac{Q_{i,j}}{2^b - 1} \rightarrow E_\nu(\lambda) \text{ d}\lambda = \frac{V_{\text{ref}} Q_{i,j}}{St_e 2^b} \quad (6.2)$$

The shape of the illuminant spectrum has to be known, as well as how temperature affects its shape. Additionally, directional, spatial and temporal effects that contribute have to be taken into consideration if an accurate measurement is to be made. If the volume of radiation can be determined with this calibration, the local effective ion charge  $Z_{\text{eff}}$  could be estimated. The analysis, however, of the volume is strongly dependent on the plasma configuration, and its derivation is not in the scope of this project.

# Appendix A

## Database structure

All the videos are structurally indexed in a database. The database consists of tables that each hold fields of data corresponding to a particular subject. The videos are labelled with an id, which is used to correlate data from different tables. This database could be included in the main TCV database, to provide extra resources for future research teams.

### A.1 SQL and databases

SQL (*Structured Query Language*) is the standard language for databases. It was chosen for this work because of dynamic features – like derived columns – and superior flexibility over an excel worksheet. For example it is able to update many rows at once with a single query.

A database is a collection of tables, each of which contains data of a different format and subject to keep distinctions clear. Tables contain headers that describe what goes into their respective columns and have to be carefully defined so that there is no unnecessary overhead, and it is ensured that no faulty data enters the table. These headers have properties like a name, type, length, a default value, flags and extra options.

The *name* field carries the name of the table header and is used to point to the column. The *type* field describes what data type is accepted, any other type will be rejected. The *size* field denotes how much bytes can be stored. The flags that are used here are the *unsigned* and the *allow NULL* flags: The *unsigned* flag denotes that the integer value is stored without a sign bit so that no negative values are allowed and the amount of possible positive numbers goes up by a factor of 2. The *allow NULL* flag allows the field to be left empty. *NULL* is an SQL keyword meaning ‘nothing’. The `PRIMARY_KEY` value appoints that field as the unique identifier for the table, and is required to distinguish rows and keep them unique. `AUTO_INCREMENT` will automatically increment the field from the last value.

## A.2 Events

This table solely contains boolean flags of which events are observed in the recording with its corresponding id. The structure is displayed in Table A.1. Once fully populated, it is possible to quickly search for videos that contain specific events by searching: The query `SELECT shot_id FROM events WHERE intensity_shift=1` will return the shot\_ids of the records in which the intensity shift flag is set to 1.

In the future, this table may be transposed to a different format where event in question is also appointed a frame interval in which the event occurs. This allows for quickly extracting events from many recordings for future research.

Table A.1: The structure of the events table. `shot_id` carries the **PRIMARY\_KEY** and the **AUTO\_INCREMENT** attributes in addition. The names are arbitrary and are dependent on orientation of the image.

| Field                        | Type     | Length | Unsigned | Allow NULL | Default |
|------------------------------|----------|--------|----------|------------|---------|
| <code>shot_id</code>         | INT      | 11     | 1        |            |         |
| <code>afterglow</code>       | TINYINT  | 1      | 1        |            | 0       |
| <code>alternation</code>     | TINYINT  | 1      | 1        |            | 0       |
| <code>artifacts</code>       | TINYINT  | 1      | 1        |            | 0       |
| <code>bright</code>          | TINYINT  | 1      | 1        |            | 0       |
| <code>intensity_shift</code> | TINYINT  | 1      | 1        |            | 0       |
| <code>death_flash</code>     | TINYINT  | 1      | 1        |            | 0       |
| <code>fail</code>            | TINYINT  | 1      | 1        |            | 0       |
| <code>faint</code>           | TINYINT  | 1      | 1        |            | 0       |
| <code>feign_death</code>     | TINYINT  | 1      | 1        |            | 0       |
| <code>flash</code>           | TINYINT  | 1      | 1        |            | 0       |
| <code>leg_extend</code>      | TINYINT  | 1      | 1        |            | 0       |
| <code>plane</code>           | TINYINT  | 1      | 1        |            | 0       |
| <code>pulsing</code>         | TINYINT  | 1      | 1        |            | 0       |
| <code>roll_down</code>       | TINYINT  | 1      | 1        |            | 0       |
| <code>roll_up</code>         | TINYINT  | 1      | 1        |            | 0       |
| <code>notes</code>           | TINYTEXT | 1      |          | 1          |         |

### A.3 Metadata

Metadata is data corresponding to a file that is *not* the main content. For example creation date, resolution and frame rate. The metadata table structure can be viewed in Table A.2. The data from this table can be processed and/or parsed without supervision and has been useful in speeding up the indexing process: The ‘empty’ field marks the files to be excluded from examination, the ‘first’ and ‘last’ fields have been used to truncate monochrome frames from the beginning and end of the video, and the ‘size’ field aided in selecting an appropriate storage overhead size.

Table A.2: The structure of the metadata table. `shot_id` carries the `PRIMARY_KEY` and `AUTO_INCREMENT` attributes.

| Field                     | Type     | Length | Unsigned | Allow NULL | Default |
|---------------------------|----------|--------|----------|------------|---------|
| <code>shot_id</code>      | INT      | 11     | 1        | 0          |         |
| <code>camera_model</code> | VARCHAR  | 35     | 1        | 1          |         |
| <code>xres</code>         | SMALLINT | 4      | 1        | 0          |         |
| <code>yres</code>         | SMALLINT | 4      | 1        | 0          |         |
| <code>bit_depth</code>    | TINYINT  | 2      | 1        | 0          |         |
| <code>exposure</code>     | SMALLINT | 5      | 1        | 1          | NULL    |
| <code>date</code>         | DATETIME |        | 1        | 1          | NULL    |
| <code>fps</code>          | SMALLINT | 5      | 1        | 1          | NULL    |
| <code>frames</code>       | INT      | 11     | 1        | 1          | NULL    |
| <code>first</code>        | INT      | 11     | 1        | 1          | NULL    |
| <code>last</code>         | INT      | 11     | 1        | 1          | NULL    |
| <code>duration</code>     | DOUBLE   |        | 1        | 1          | NULL    |
| <code>empty</code>        | TINYINT  | 1      | 1        | 0          | 0       |
| <code>size</code>         | INT      | 11     | 1        | 1          | NULL    |
| <code>cams</code>         | TINYINT  | 1      | 1        | 1          | NULL    |

## A.4 Raw

Unprocessed or *raw* files are stored in this table, almost 1000 videos have been recorded and can be as large as 1 GiB<sup>1</sup>. To accumulate all this data in binary form, 4 TiB of storage overhead is required (A.1). This calls for compression, which is beyond the scope of this report.

$$1000 \cdot \frac{(2^{32} - 1) \text{ bytes}}{2^{30} \text{ bytes per GiB}} = 4.0 \text{ TiB} \quad (\text{A.1})$$

Table A.3: The structure of the raw table. `LONGBLOB` stands for LONG Binary Large Object and can hold  $2^{32} - 1$  bytes (4 GiB) of data and is used to store the file. `shot_id` carries the `PRIMARY_KEY` and `AUTO_INCREMENT` attributes in addition.

| Field                | Type                  | Length | Unsigned | Allow NULL |
|----------------------|-----------------------|--------|----------|------------|
| <code>shot_id</code> | <code>INT</code>      | 11     | 1        |            |
| <code>data</code>    | <code>LONGBLOB</code> |        |          | 0          |

---

<sup>1</sup>The *i* in the prefix denotes binary prefixes rather than decimal 1 GiB = 1024<sup>3</sup> bytes whereas 1 GB = 1000<sup>3</sup> bytes.

## Appendix B

# Camera system

The cameras are inserted in vision holes in the wall of the TCV vessel. To protect the cameras from radiation and heat from the plasma, relay optics are inserted between the camera and hole. Relay optics consist of tubes and lenses to redirect and focus the light elsewhere.

The imaging chip in the camera consists of a pixel grid that are either a complementary metal-oxide semiconductor (CMOS) or charge coupled device (CCD) chip. The sensitivity is specified in  $Vlux^{-1} s^{-1}$ , and with dimensional analysis the formula for calculating the voltage on the pixel can be derived (6.2), which can then be used in an attempt to derive the original intensity distribution.

The frame rate of these cameras is around the order of  $10^3$  frames per second (fps). This, together with the resolution and the bit depth – amount of bits per colour channel – sets a measure for the bandwidth that is required

$$B = F \cdot R \cdot b \cdot C \tag{B.1}$$

where  $F$  is the frame rate,  $R$  the resolution ( $x \cdot y$ ),  $b$  the amount of bits per colour channel and  $C$  the amount of colour channels. For most cases in this work  $F = 200$ ,  $R = 400^2$ ,  $b = 10$  and  $C = 1$  which means that  $B = 40 \text{ Mb s}^{-1}$  Mbs or  $38 \text{ MiB s}^{-1}$ . With more advanced research cameras like one with  $1280 \times 1024$  px resolution at full color (3 channels) and 1000 fps, it is not difficult to exceed a gigabyte per second bandwidth.

Hyper imaging spectroscopy is a technique consisting of a multiple camera configuration that captures light from a common source but is filtered. For example: Light from the plasma travels through relay optics and enters an optical system in which red, green and blue light are decoupled. These different colours are then directed to the three different cameras. With such a configuration it is possible to resolve real-time image data spectrally and spatially.

# Bibliography

- [1] B. Lipschultz, B. LaBombard, E.S. Marmor, M.M. Pickrell, J.L. Terry, R. Watterson, and S.M. Wolfe. Marfe: an edge plasma phenomenon. *Nuclear Fusion*, 24(8):977, 1984.
- [2] D. J. C. MacKay. *Sustainable Energy – without the hot air*. UIT Cambridge Ltd., PO Box 145, Cambridge, CB4 1GQ, England, Dec 2008.
- [3] <https://www.iter.org/factsfigures>.
- [4] J. Wesson and D.J. Campbell. *Tokamaks*. Oxford University Press, 2011.
- [5] M Keilhacker. H-mode confinement in tokamaks. *Plasma Physics and Controlled Fusion*, 29(10A):1401, 1987.
- [6] G. Hommen, M. de Baar, P. Nuij, G. McArdle, R. Akers, and M. Steinbuch. Optical boundary reconstruction of tokamak plasmas for feedback control of plasma position and shape. *Review of Scientific Instruments*, 81(11):13, Nov 2010.
- [7] G. Hommen, M. de Baar, J. Citrin, H. J. de Blank, R. J. Voorhoeve, M. F. M. de Bock, and M. Steinbuch. A fast, magnetics-free flux surface estimation and q-profile reconstruction algorithm for feedback control of plasma profiles. *Plasma Physics and Controlled Fusion*, 55:025007, Feb 2013.
- [8] G. Hommen, M. de Baar, B. P. Duval, Y. Andrebe, H. B. Le, M. A. Klop, N. J. Doelman, G. Witvoet, M. Steinbuch, and TCV team. Real-time optical plasma boundary reconstruction for plasma position control at the tcv tokamak. *Nuclear Fusion*, 54(7):073018, 2014.